Photoexcited charge carrier dynamics and electronic properties of two-dimensional MXene, Nb_2CT_x

2D Materials

RECEIVED
18 January 2024

REVISED
22 April 2024

ACCEPTED FOR PUBLICATION
29 May 2024

PUBLISHED
12 June 2024

PAPER

Photoexcited charge carrier dynamics and electronic properties of two-dimensional MXene, Nb_2CT_x

Andrew M Fitzgerald[1,7], Emily Sutherland[1,7], Tarek Ali El-Melegy[2,3], Mary Qin Hassig[3], Julia L Martin[4], Erika Colin-Ulloa[1], Ken Ngo[5], Ronald L Grimm[4], Joshua R Uzarski[5], Michel W Barsoum[3], N Aaron Deskins[6], Lyubov V Titova[1,*] and Kateryna Kushnir Friedman[1,*]

[1] Department of Physics, Worcester Polytechnic Institute, Worcester, MA, United States of America
[2] Department of Mechanical Engineering, The British University in Egypt, Cairo, Egypt
[3] Department of Materials Science and Engineering, Drexel University, Philadelphia, PA, United States of America
[4] Department of Chemistry and Biochemistry, Worcester Polytechnic Institute, Worcester, MA, United States of America
[5] US Army DEVCOM Soldier Center, Natick, MA, United States of America
[6] Department of Chemical Engineering, Worcester Polytechnic Institute, Worcester, MA, United States of America
[7] Equal contribution.
[*] Authors to whom any correspondence should be addressed.

E-mail: ltitova@wpi.edu and kkushnir@wpi.edu

Keywords: MXenes, 2D materials, terahertz spectroscopy, density functional theory, Nb2C

Supplementary material for this article is available online

Abstract

Two-dimensional, 2D, niobium carbide MXene, Nb_2CT_x, has attracted attention due to its extraordinarily high photothermal conversion efficiency that has applications ranging from medicine, for tumor ablation, to solar energy conversion. Here, we characterize its electronic properties and investigate the ultrafast dynamics of its photoexcitations with a goal of shedding light onto the origins of its unique properties. Through density functional theory, DFT, calculations, we find that Nb_2CT_x is metallic, with a small but finite DOS at the Fermi level for all experimentally relevant terminations that can be achieved using HF or molten salt etching of the parent MAX phase, including –OH, –O, –F, –Cl, –Br, –I. In agreement with this prediction, THz spectroscopy reveals an intrinsic long-range conductivity of $\sim$60 Ω^{-1} cm^{-1}, with significant charge carrier localization and a charge carrier density ($\sim 10^{20}$ cm^{-3}) comparable to Mo-based MXenes. Excitation with 800 nm pulses results in a rapid enhancement in photoconductivity, which decays to less than 25% of its peak value within several picoseconds, underlying efficient photothermal conversion. At the same time, a small fraction of photoinjected excess carriers persists for hundreds of picoseconds, and can potentially be utilized in photocatalysis or other energy conversion applications.

1. Introduction

Discovered in 2011, MXenes are a class of two-dimensional, 2D, transition metal carbides, nitrides, and carbonitrides. These materials share the general chemical formula $M_{n+1}X_nT_x$, where M is an early transition metal, X is carbon or nitrogen, n takes on a value from 1–4, and T_x stands for the surface terminations, such as –OH, –O, or –F. The latter form when the A-layer, typically Al, is selectively etched away from their parent MAX-phases [1]. Several different MXene materials have displayed exceptional properties, including high conductivity, record high volumetric capacitances, nonlinear optical effects, and efficient photothermal conversion, suggesting the potential for applications in electromagnetic interference shielding [2–4], energy storage [5–13], optoelectronic and photonic devices [14–20], electrochemical sensors [21, 22], and even photothermal cancer treatments [23–27].

A member of MXene family, niobium carbide, Nb_2CT_x, was discovered in 2013, [8] and has since been drawing attention for its high photothermal conversion efficiency [23, 24, 28, 29], good biocompatibility [23], high reversible capacity (when integrated into battery anodes or electrodes) [8, 9, 11, 13], and nonlinear optical properties [19, 20, 30], rendering this MXene potentially attractive for

applications in photothermal cancer therapy, antibacterial sterilization, batteries, and optoelectronic and photonic devices. Despite numerous experimental and computational studies, the electronic properties of Nb_2CT_x with different surface terminations, the nature of conductivity and the behavior of photoexcitations in this MXene are not well described or characterized. For instance, unlike the highly conductive $Ti_3C_2T_x$, Ti_2CT_x, or V_2CT_x [18, 31], Nb-based MXenes such as Nb_2CT_x and $Nb_4C_3T_x$ have been reported to have low intrinsic electrical conductivities, raising the question of whether these MXenes possess a metallic or semiconducting nature [32]. In our recent work, we demonstrated that Nb_2CT_x with mixed O and OH terminations exhibits a surface plasmon resonance despite having a low intrinsic free carrier density, pointing to its metallic nature [33].

In this study, we investigate the electrical and optical properties of Nb_2CT_x by combining Density Functional Theory (DFT) calculations of its electronic structure, as a function of surface terminations, with experimental measurements of intrinsic and photoexcited conductivities using terahertz (THz) spectroscopy. Recent DFT studies uncovered that the surface terminations, T_x, play a defining role in determining whether or not a small gap opens in the band structure of Nb-based MXenes [34, 35]. Here, we model Nb_2CT_x with a number of surface terminations. We study Nb_2CT_x with hydroxyl, oxygen, or a combination of these terminations that occur when it is fabricated by HF etch of the parent Nb_2AlC MAX phase followed by delamination in a NaOH, TMAOH or TBAOH solution [8, 36, 37] which matches the film we use for experiments. In addition, we investigate $T_x = N$, which has previously been predicted to result in opening of a band gap [34], as well as halogen terminations that result from etching of MAX phase using molten salts [38–42]. We find that Nb_2CT_x is metallic for all surface terminations with the exception of nitrogen. In agreement with this, THz-TDS shows that Nb_2CT_x sheets have an intrinsic free carrier density on the order of 10^{20} cm^{-3} and considerable intra-sheet carrier mobility of $\sim$30 cm^2 V^{-1} s^{-1}, comparable to other MXenes [31, 43–45]. Long-range transport in macroscopic films is limited by nanosheet boundaries that suppress the inter-sheet mobility more than ten-fold to 2.4 ± 0.4 cm^2 V^{-1} s^{-1}. Finally, we find that photoexcitation transiently enhances Nb_2CT_x conductivity, as has been reported in other metallic MXenes with intrinsic carrier densities $\sim 10^{20}$ cm^{-3} or below, such as $Mo_2Ti_2C_3T_x$, $Mo_2TiC_2T_x$ or $Nb_4C_3T_x$, and in contrast to MXenes with high carrier densities $>10^{21}$ cm^{-3}, such as $Ti_3C_2T_z$, where conductivity is suppressed as rapid lattice heating results in lower carrier mobility [31, 32, 43–45]. We find that most of the optically injected carriers recombine and are trapped at the defect states within one picosecond after excitation, while a small fraction persists for tens and hundreds of picoseconds. Thus, ultrashort photoexcited carrier lifetime may be utilized in high-speed photoelectronic devices as another potential application of this MXene.

2. Methods

2.1. Synthesis

2.1.1. MAX phase synthesis

To synthesize the Nb_2AlC phase, first, powders of Nb (99.8% purity, 1–5 μm), Al (99.5% purity, $<$ 44 μm, $-$325 mesh), and C (99% purity, $<$ 48 μm, $-$300 mesh), all acquired from Alfa Aesar, were mixed in a 2:1.1:1 molar ratio in a polyethylene jar with zirconia milling balls, 5–20 mm in diameter. Excess Al compensates for evaporation and aluminothermic reduction of native metal oxides. The mixed powders were ball-milled (U.S Stoneware, OH, USA) for 24 h at 70 rpm and then transferred to an alumina, Al_2O_3, boat, which was placed inside an Al_2O_3 tube furnace and heated under flowing argon, Ar, (flow rate 15 SCCM) to 1600 °C for 4 h at a heating rate of 3 °C /min. The resulting solid was then drilled into a powder and sieved through a 400 mesh to obtain a powder with a particle size of less than 38 μm.

2.1.2. MXene etching

Multilayered (ML) Nb_2CT_X flakes were obtained by etching 1 g of Nb_2AlC powder in 10 ml of HF solution (50 wt.%, Acros Organics, Morris Plains, USA) and stirring (PC-420D, Corning, NY, USA) for 96 h at 55 °C and 400 rpm. The resulting slurry was decanted into a 50 ml centrifuge tube, and deionized, DI, water (18 MΩ cm, Milli-Q, Merck KgaA, Darmstadt, Germany) was added to fill the remaining volume. The centrifuge tube was then sealed and shaken for 60 s (Fisherbrand™ Analog Vortex Mixer, Hampton, NH, USA), after which it was centrifuged at 3500 rpm for 120 s (Sorvall ST 16, Thermo Fisher Scientific, MA, USA). The supernatant was discarded, then DI water was added, and washing was repeated until the pH of the supernatant reached ≈7. After washing, the MXene-containing sediment was collected and air dried.

2.1.3. MXene delamination

To delaminate the Nb_2CT_X MLs into single to few layers, ≈0.2 g of the ML from the washing process was dispersed in 2 ml of tetrabutylammonium hydroxide, TBAOH, (40 wt.% in water, Alfa Aesar, MA, USA) and shaken in for 15 min. The mixture was washed twice with ethanol (200-proof, Fisher Scientific, NH, USA), followed by a final DI water washing step. After washing off excess TBAOH, the sediments were redispersed in fresh DI water, and the mixture was then sonicated (Model 505 Sonic Dismembrator, 500 W, Fisher Scientific, NH, USA) under bubbling Ar flow for 1 h with 30 s/30 s on/off cycles at 75% amplitude. To avoid oxidation, the bath temperature was

maintained below 20 °C using ice. The solution was centrifuged for 1 h at 3500 rpm, the supernatant was decanted into a fresh centrifuge tube, while the residual sediment containing any unetched MAX or non-delaminated MXene was discarded.

2.1.4. MXene deposition

The resultant Nb_2CT_x colloid was deposited by a gravity-feed, compressed-gas-propelled commercial airbrush (Master Airbrush, G233) onto IR-grade quartz to produce a thin film of Nb_2CT_x. Spray depositions utilized ∼0.25 ml of a 1:10 aqueous dilution of the concentrated Nb_2CT_x colloid. Routine cleaning of the airbrush body and components utilized dilute, aqueous glacial acetic acid (AcOH, 99.7%, Alfa Aesar) was carried out as follows. Components in frequent contact with Nb_2CT_x material including the needles, fluid tips, and reservoir were sonicated in the aqueous, dilute acetic acid and rinsed with copious amounts of water in between subsequent depositions. This process results in a multilayer film consisting of many individual nanoflakes with sub-μm lateral dimensions. In such films, the transport properties result from an interplay of short-range, intra-flake carrier motion and long-range, inter-flake hopping transport [32, 44]. Using a stylus profilometer, we found the thickness of this MXene film to be 185 ± 11 nm.

2.2. Density functional theory (DFT)

All DFT calculations were performed using the Vienna ab initio Simulation Package (VASP) [46–49]. The generalized gradient approximation exchange correlation functional by Perdew, Burke, and Ernzerhof (PBE) [50] was utilized for our calculations. Projector augmented wave (PAW) pseudopotentials [51, 52] described the core electron states. The cutoff energy for valence electron wavefunctions was set to 450 eV. The Brillouin zone was sampled with a Γ-centered mesh with 3 × 3 × 1 *k*-points. During structure relaxation, calculation convergence criteria for energies and forces were set to 10^{-5} eV and 0.002 eV Å^{-1}, respectively. The Gaussian smearing method was used with a width of 0.25 eV, which was chosen to optimize the smoothness of density of states (DOS) curves. To further confirm the metallic nature and or identify potential band gap, DOS calculations were performed using the HSE06 exchange correlation functional [53] with a smearing width of 0.05 eV (recommended by the VASP documentation for semiconductors). Since HSE06 calculations are so time-consuming, we used the PBE geometries for the HSE06 calculations. Post-processing extraction of DOS values and band structure from VASP simulations was carried out using the VASPKIT package [54].

We studied the electronic structure for 3 × 3 supercells of Nb_2CT_2 MXenes with T = O, F, OH, N, Cl, Br, or I. We modeled Nb_2CT_2 MXenes with mixed OH/O terminations in a 1:1 ratio, and mixed OH/F terminations in 1:1, 2:1 and 5:1 ratios. Previous literature suggests that mixed terminations may be randomly distributed and depend on the synthesis method [55–57]. Accordingly, we modeled mixed termination MXenes also with random configurations, and having symmetry between the top and bottom surfaces maximized (see figure S5). MXenes generally have trigonal symmetry with terminations located either in the hollow sites above metal atoms (h_M) as in figures 1(a) and (b), or in the hollow sites above X (carbon or nitrogen) atoms (h_X) as in figures 1(c)and (d). Sample calculations for Nb_2CF_2, and $Nb_2C(OH)_2$, predict these structures to have an energetic preference for the h_M configuration, which is consistent with the most stable configuration predicted for Nb_2CT_2 in other studies [58, 59]. Therefore, in this work all structures were modeled with trigonal symmetry and the h_M termination configuration. To avoid interlayer interactions, the cell length along the *z* direction was set to 20 Å.

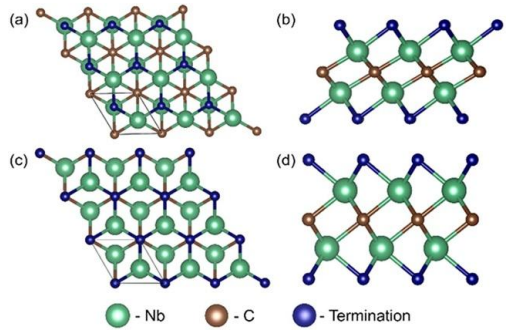

Figure 1. Top (left) and side (right) views of Nb_2CT_X MXenes modeled in this work. The h_M configuration is shown in (a), (b) and the h_X configuration is shown in (c), (d). Green spheres are Nb atoms, brown spheres are carbon, and blue spheres are representative of terminations. The diamond outline shown in the top view outlines a single unit cell. Figures for all modeled structures are given in supporting information, SI.

2.3. Terahertz spectroscopy

The intrinsic conductivity of Nb_2CT_x in the 0.25–2.5 THz range was investigated using THz time-domain spectroscopy (THz-TDS) in transmission mode [31, 44, 60–62]. THz-TDS is a non-contact, all-optical technique that allows measurement of complex, frequency-resolved conductivity. THz probe pulses were generated in a 1 mm-thick ZnTe [100] crystal upon photoexcitation with 800 nm, 100 fs pulses from an amplified Ti: Sapphire laser. The bandwidth of the generated THz pulses spans in the 1–10 meV range. Off-axis parabolic mirrors were used to focus the THz pulses onto the ∼ 1.5 mm spot on the sample at normal incidence and to collect transmitted THz pulses, directing them to the detector. They were detected by another 1 mm-thick [100] ZnTe crystal using electro-optic sampling.

Analyzing the amplitude and phase of the THz pulse through the substrate and sample in the frequency domain yields the complex frequency-resolved conductivity of the material [63, 64].

In addition, time-resolved THz spectroscopy (TRTS) was used to study the effects of photoexcitation with 800 nm (1.55 eV), 100 fs pulses [60, 65–68]. The optical excitation beam was directed on to the sample through a 5 mm aperture in the parabolic mirror that focused the THz probe pulse onto the sample. A larger optical excitation spot size (≈5 mm) ensured uniform illumination of the entire THz probe pulse spot on the MXene sample. A mechanical delay line was used to control the arrival time of the THz probe pulse relative to the optical excitation pulse.

3. Results and discussion

3.1. Density functional theory (DFT)

Earlier studies on Nb_2CT_x have reported a negligibly low conductivity for this MXene, [18] leading to the hypotheses that Nb-based MXenes may be semiconducting rather than metallic in nature. However, observed plasmonic properties suggest the presence of a nonzero, and measurable, concentration of free charge carriers [33]. Accordingly, we used DFT to model the electronic properties of Nb_2CT_2 in order to establish the nature of the conductivity of these materials.

Initial band structure and DOS calculations, using the PBE functional, revealed a metallic nature for bare Nb_2C, which is retained upon adsorption of O, F, OH, Cl, Br, and I groups (see figure 2). Further DOS calculations using the HSE06 functional, which is known to be more accurate than PBE for predicting conductive nature, confirm that these MXenes are metals (see SI for figures). Our results are in agreement with literature [35, 58, 59, 69, 70]. Additionally, our simulations of Nb_2CT_2 with mixed OH/F and O/OH terminations indicate that the metallic nature is also preserved when multiple termination types are present, independent of their ratio (see SI for figures S6 and S7). In the case of nitrogen, N, terminations, however, Nb_2CT_x transitions to a semiconductor with a band gap of 0.25 eV with PBE and 0.66 eV with HSE06, which is in agreement with previous studies [34, 71, 72]. The band gap may be difficult to see in the DOS due to the smearing applied to the DOS. However, the band gap in Nb_2CN_2 is evident from the band structure (figure 2), as well as examining the energy eigenvalues in the OUTCAR file.

Partial DOS, PDOS, curves for Nb_2CT_2, shown in figure 2 and SI, reveal that the electronic states of Nb atoms dominate the electronic structure near the Fermi level, E_F, while the C, F, O, Cl, Br and H atoms have much less contribution. This indicates that the d-orbitals of Nb atoms are responsible for the metallic nature of Nb_2CT_x with Cl, Br, O, F, and/or OH terminations. For Nb_2CN_2, however, Nb–N bonding produces a shift in the E_F such that a band gap is opened. Nb_2CI_2 has significant contributions from both Nb and I atoms at E_f, indicating that this material may have notably higher electrical conductivity as compared to the other Nb_2CT_2 MXenes considered in this study. MXenes with Cl, Br, or I terminations are rare, however, as they are typically synthesized using molten salts [38–42]. Future studies may examine these materials in detail.

As previously reported for Nb_2CT_x synthesized as described above, x-ray photoelectron spectroscopy (XPS) shows that Nb_2CT_x has much more surface oxides than $Ti_3C_2T_x$ or $Mo_2Ti_2C_3T_x$, and the only terminations present are O and OH. No measurable F was detected, probably due to the removal of fluorine during TBAOH treatment [36]. Considering only the MXene-ascribable components, the XPS-determined Nb:C ratio of 2:0.9 is in good agreement with the expected 2:1 stoichiometric ratio. As noted above, for the O and OH terminations, DFT unambiguously predicts the metallic nature of Nb_2CT_x.

3.2. THz time-domain spectroscopy (THz-TDS)

Figure 3(a) shows the THz pulses transmitted through the quartz substrate alone and through the 185 ± 11 nm thick Nb_2CT_x film deposited on top of the quartz substrate. The inset shows the amplitude spectra of the same THz pulses in the frequency domain. The frequency-dependent, complex conductivity of Nb_2CT_x can be calculated from the amplitude and phase of the THz pulses that have been transmitted through the sample on the quartz substrate and through the quartz substrate alone using

$$\frac{\tilde{E}_{\text{sample}}(\omega)}{\tilde{E}_{\text{substrate}}(\omega)} = \frac{n+1}{n+1+Z_0\tilde{\sigma}(\omega)}, \tag{1}$$

where n is the refractive index of the quartz substrate in the THz frequency range (∼2.156, assumed here to be constant as reported variation is <1% within the 0.25–2.5 THz range) [73], Z_0 is the impedance of free space (377 Ω), and $\tilde{E}_{\text{sample}}(\omega)$ and $\tilde{E}_{\text{substrate}}(\omega)$ are the electric fields of the THz pulses transmitted through the sample and substrate together and through the substrate alone [31, 60, 74].

Figure 3(b) plots the real (σ_1) and imaginary (σ_2) parts of this intrinsic conductivity as functions of frequency. To model the complex conductivity, we employ the Drude−Smith model, a modification of the free carrier Drude conductivity that incorporates the effects of carrier localization over distances comparable to their mean free path by the disorder and grain boundaries or, in this case, the boundaries of individual Nb_2CT_x nanosheets [44, 61, 75–77].

The Drude–Smith model for complex conductivity is given by

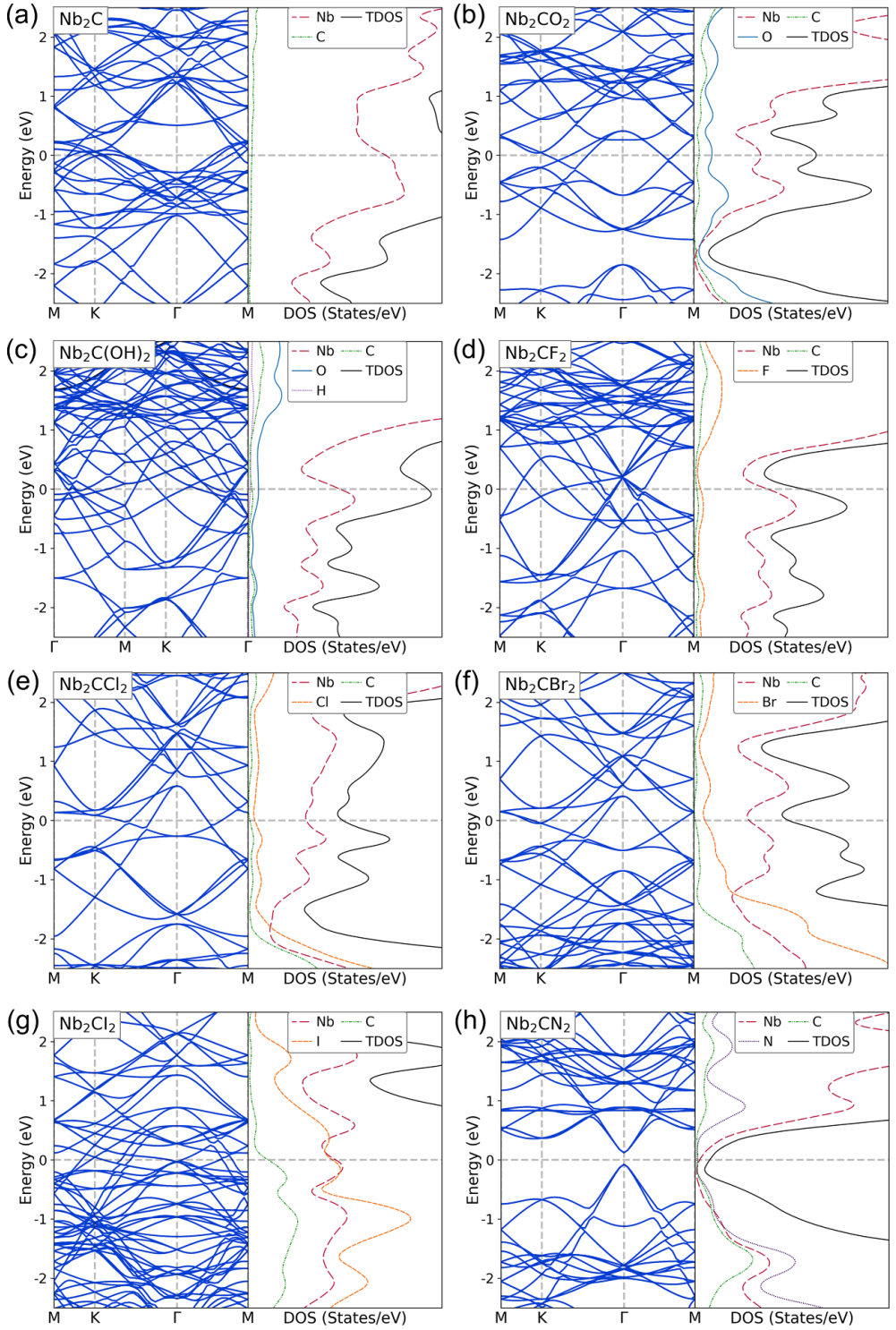

Figure 2. Band structure and DOS plots for Nb_2C (a), Nb_2CO_2 (b), $Nb_2C(OH)_2$ (c), Nb_2CF_2 (d), Nb_2CCl_2 (e), Nb_2CBr_2 (f), Nb_2CI_2 (g), and Nb_2CN_2 (h) as calculated by DFT using the PBE exchange correlation functional. These results predict Nb_2CN_2 to be semiconducting, and all others to be metallic. All DOS plots are scaled identically. Energies are shown relative to the Fermi energy (0 eV).

$$\tilde{\sigma}(\omega) = \frac{\sigma_0}{1 - i\omega\tau_{DS}}\left(1 + \frac{c}{1 - i\omega\tau_{DS}}\right), \quad (2)$$

$$\sigma_0 = \frac{Ne^2\tau_{DS}}{m^*}, \quad (3)$$

where c is the localization parameter, τ_{DS} is carrier scattering time, and σ_0 is given by

where N is the intrinsic charge carrier density and m^* is the carrier effective mass [44, 78]. In the

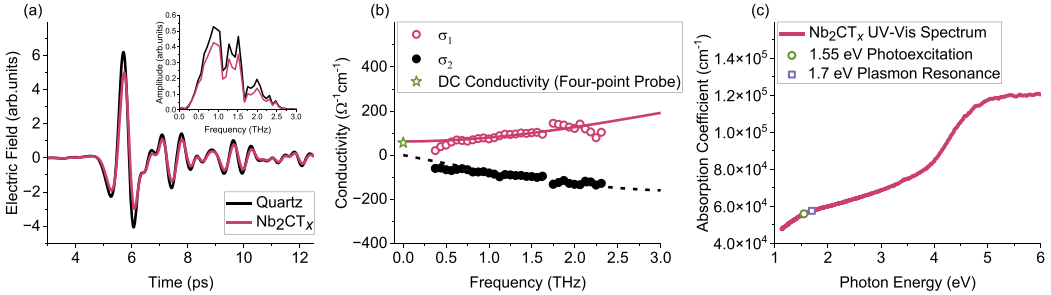

Figure 3. (a) THz waveforms in the time-domain transmitted through quartz (black line) alone and through a thin-film sample of Nb_2CT_x deposited onto the quartz substrate (magenta line). Inset plots THz amplitude in the frequency-domain. (b) Real (σ_1) and imaginary (σ_2) intrinsic conductivities of Nb_2CT_x. Lines represent fits to the Drude–Smith model for complex conductivity (solid line—fit to real part of model; dashed line—fit to imaginary part of model). Green star represents DC conductivity measured by four-point probe. Experimental error in these measurement is smaller than the symbol size. (c) Optical absorption coefficient of Nb_2CT_x in UV-near IR spectral range. Photon energy used in TRTS measurements (1.55 eV) is shown as an open circle. Also shown is a center photon energy of a plasmon resonance reported earlier in Nb_2CT_x [29], at 1.7 eV.

Drude–Smith model, the localization parameter can take on a value between 0 and −1. For $c = 0$, charge carriers move throughout a sample entirely unimpeded; for $c = -1$, the charge carriers' movement is entirely suppressed or localized.

Lines in figure 3(b) represent the global fit of both real and imaginary intrinsic conductivity to equation (2).

Note that the complexity of the Fermi surface in Nb_2CT_x, that can be inferred from the band structure diagrams in figure S8, complicates calculation of the effective carrier mass necessary for extracting the carrier density from the Drude–Smith fitting parameters. For the sake of obtaining an estimate of Nb_2CT_x carrier density, we assume here $m^* = m_e$, and in doing so, we find that $N = (1.6 \pm 0.3) \times 10^{20}$ cm^{-3}.

The charge carrier density we find here is comparable to that of $Mo_2Ti_2C_3T_x$ and $Mo_2TiC_2T_x$ (where Li *et al* also approximated the effective carrier mass to the mass of a free electron) [44] but about two orders of magnitude lower than that of $Ti_3C_2T_x$ [31]. For this sample the localization parameter, $c = -0.92 \pm 0.01$, is close to −1, suggesting that charge carriers are highly localized over distances comparable to their mean free path, either due to defects or the edges of individual nanoflakes. As a result, static (or DC) conductivity can be estimated by extrapolating the real part of the Drude–Smith model out to 0 THz:

$$\sigma_{DC} = \mathrm{Re}\left[\tilde{\sigma}(0)\right] = 62 \pm 15\ \Omega^{-1}\mathrm{cm}^{-1}. \quad (4)$$

We find that Nb_2CT_x has a low, but finite, intrinsic conductivity of 62 ± 15 Ω^{-1} cm^{-1}, which is about two orders of magnitude lower than other MXenes like $Ti_3C_2T_x$ [31]. To corroborate this estimate of conductivity, we also measured this sample's conductivity using a four-point probe technique [79, 80]. At 56 ± 11 Ω^{-1} cm^{-1}, the DC conductivity measured was in good agreement with the THz measurement. Although this is low, it is still a measurable, nonzero quantity.

To understand the intrinsic conductivity, we calculate the intrinsic charge carrier mobility within individual nanoflakes from the Drude–Smith scattering time, τ_{DS}, as

$$\mu_{\mathrm{intrinsic}} = \frac{e\tau_{DS}}{m^*}. \quad (5)$$

Again assuming $m^* = m_e$, and using $\tau_{DS} = 17 \pm 2$ fs from the Drude–Smith fit, we estimate the intrinsic carrier mobility of this sample to be 30 ± 4 cm^2 V^{-1} s^{-1}. From here, we can estimate the long-range carrier mobility assuming,

$$\mu_{\mathrm{long-range}} = \mu_{\mathrm{intrinsic}}(1 + c), \quad (6)$$

which results in a long-range charge carrier mobility of 2.4 ± 0.4 cm^2 V^{-1} s^{-1}. The significant disparity between intrinsic and long-range conductivities suggests—like in our previous work—that charge carrier mobility is impeded by the boundaries of the nanoflakes comprising our material [31, 44].

3.3. Time-resolved terahertz spectroscopy (TRTS)

Figures 4(a) and (b) both show the negative change in THz peak transmission following a 1.55 eV photoexcitation for three different fluences. As shown in figure 3(c), the energy of this photoexcitation is quite close to the 1.7 eV plasmon resonance observed by Colin–Ulloa *et al* in Nb_2CT_x [33]. In the limit of small changes ($-\Delta T/T < 20\%$), this is proportional to transient photoconductivity ($\Delta\sigma$). Figure 4(a) shows the early time window (within the first 10 ps after photoexcitation, together with the photoexcited excess carrier densities, extracted from the Drude–Smith fits to transient photoconductivity spectra at different times after excitation, as discussed later, while figure 4(b) displays normalized transient photoconductivity over an extended time window (as far out as 250 ps after photoexcitation). We find that photoexcitation of Nb_2CT_x results in a rapid onset of enhanced photoconductivity as interband excitations

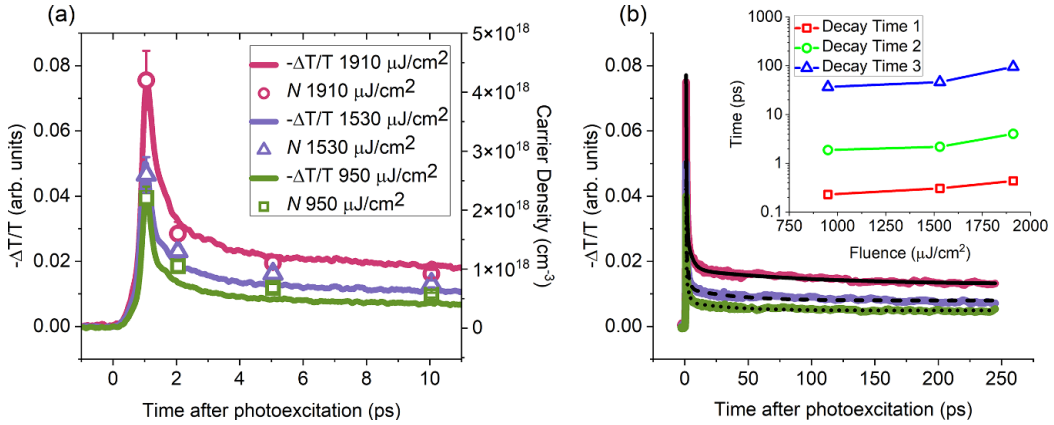

Figure 4. TRTS pump scans of Nb_2CT_x using three different photoexcitation fluences at 1.55 eV. Each plot is fitted to a three-component exponential decay model, with solid, dashed, and dotted black lines corresponding to fluences of 950 μJ cm^{-2}, 1530 μJ cm^{-2}, and 1910 μJ cm^{-2}, respectively. Panel (a) displays TRTS pump scans ranging from 1 ps before photoexcitation to 11 ps after, while panel (b) displays time range from 1 ps before photoexcitation to 250 ps after. Inset in (b) plots the three decay times on a semi-log plot a function of fluence. Error bars are too small to include for these decay times.

inject a new population of free carriers with the excess carrier density reaching ∼10% of the intrinsic value.

Following this initial enhancement, the photoconductivity of the sample exhibits a significant decay within the first few ps (figure 4(a)). About 10%–20% of the photoinjected carriers have much longer lifetimes >250 ps (figure 4(b)). The photoconductivity decays are clearly multi-exponential, revealing the presence of multiple relaxation channels. We find they can be well-described by three-component exponential decays, with decay times given in the inset to figure 4(b). All decay times increase with excitation fluence, a hallmark of saturation or filling of the channels responsible and ruling out carrier–carrier scattering or Auger recombination as candidates for the fastest, sub-ps decay. As proposed earlier for $Nb_4C_3T_x$, trapping on the fastest decay time can be attributed to defects arising from oxidation [32]. They are presumably uniformly distributed throughout the nanosheets, allowing for fast trapping of excess carriers, and saturate with increasing injected excess carrier density. In addition to the most prominent, sub-ps decay, we observe a slightly slower decay time under 5 ps, which is followed by significantly longer decay times on the order of hundreds of ps. Those decays also show that the states responsible for the decays fill with increasing excitation fluence. We therefore ascribe them to carrier trapping at intra-nanosheet species as well as nanosheet edges.

The enhancement in conductivity that we observe in in response to photoexcitation is similar to the behavior of other MXenes including $Mo_2Ti_2C_3T_x$ [44], $Mo_2TiC_2T_x$ [44], and $Nb_4C_3T_x$ [32] but opposite to the negative photoconductivity seen in the highly conductive MXene, $Ti_3C_2T_x$ [31], where the dominant effect is heating of the intrinsic electron gas followed by a rapid increase in lattice temperature, which gives rise to a transiently reduced conductivity. In all these MXenes, both effects, injection of excess carriers and increase in carrier and lattice temperature, are present, as photoexcitation quickly heats up the crystal lattice, as evidenced by the transient broadening of the plasmon resonance peak in $Ti_3C_2T_x$, $Mo_2Ti_2C_3T_x$ and Nb_2CT_x [33]. Positive photoconductivity in $Mo_2Ti_2C_3T_x$, $Mo_2TiC_2T_x$ and Nb_2CT_x *cannot* be taken as the signature of semiconducting behavior. Rather, in metallic MXenes with sufficiently low intrinsic carrier density ($\leqslant 10^{20}$ cm^{-3}), transient increase in carrier density dominates over the transient decrease in carrier mobility.

To estimate the injected carrier density and gain additional information on their behavior, we extracted the complex, frequency-resolved photoconductivity at different points in the time (1–10 ps) after the sample had been photoexcited. Figures 5(a)–(c), show selected photoconductivity spectra at 1, 5, and 10 ps after photoexcitation for fluences of 1910 μJ cm^{-2}, respectively. Figures 5(d) and (e) and (f) plot the corresponding results for a fluence of 950 μJ cm^{-2}. Spectra at all 1, 2, 5, and 10 ps for all three fluence values studied are shown in figure S2. Like in the case of intrinsic THz conductivity, the lines in figure 5 are the global fits of the real and imaginary photoconductivity components to the Drude–Smith model. From these fits, we can once again extract a localization parameter, scattering time, and carrier density for each spectrum.

Our measurements show that different fluences of 1.55 eV photoexcitations have little to no effect on the Drude–Smith parameters. We find that the localization parameter remains mostly unchanged after photoexcitation, and remains that way for the first 10 ps thereafter, for all studied fluence values. The localization parameter was measured to be -0.91 ± 0.05 after photoexcitation, which is slightly lower than

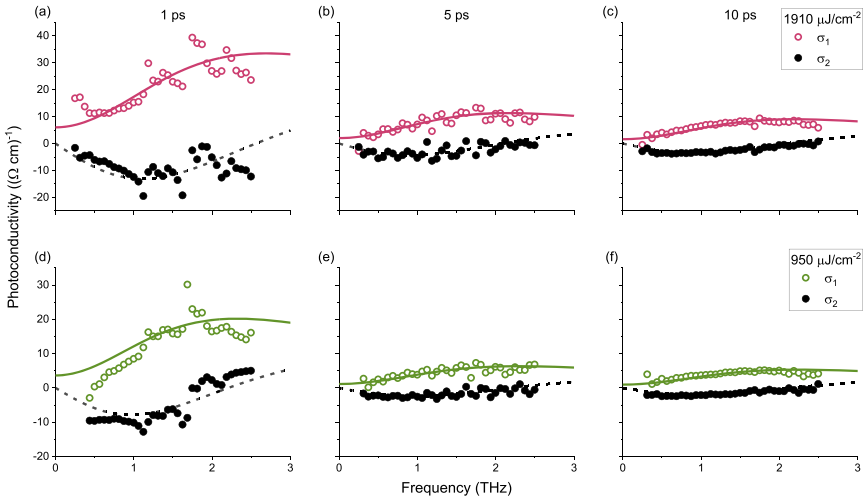

Figure 5. Photo-induced change in complex THz conductivity in Nb_2CT_x at 1, 5 and 10 ps after 1.55 eV photoexcitation with (a)–(c) fluences of 1910 μJ cm^{-2} and (d)–(f) 950 μJ cm^{-2}. Solid and dotted lines represent fits to the Drude–Smith model for complex conductivity.

the $c = -0.92 \pm 0.01$, we measure in our TDS experiments. This suggests that the movement of photoexcited charge carriers in the material is suppressed to a similar degree as the movement of the intrinsic carriers.

On the other hand, we observe that the scattering time experienced by the carriers within at least the first 10 ps after excitation is significantly longer compared to the intrinsic carrier scattering time, 65 ± 8 fs vs. 17 ± 2 fs, almost a three-fold increase. An ultrashort pulse with average photon energy of 1.55 eV injects a population of hot free electrons (holes) into delocalized bands at the energies above (below) the Fermi level, and those excess carriers appear to experience a lower scattering rate and higher mobility. As in the case of the localization parameter, excitation fluence does not impact the carrier scattering time.

Finally, the Drude–Smith fitting of the experimental photoconductivity spectra at different times after excitation allows estimation of the photoexcited excess carrier density, plotted in figure 4(a) along with $-\Delta T/T$. We find that at the peak of measured photoconductivity, photoexcitation is responsible for a maximum excess carrier density of $(4.2 \pm 0.5) \times 10^{18}$ cm^{-3}, that is at most a few percent of the intrinsic carrier density.

Also, as the carrier mobility (determined by the scattering time and the localization parameter) is unchanged over the first 10 ps, we find that the transient photoconductivity decay is determined exclusively by the trapping and recombination of excess carriers. Based on the measured absorption coefficient at 1.55 eV (5.6×10^4 cm^{-1}, figure 3(c)) and the penetration depth of ~180 nm, comparable to the film thickness, neglecting reflection losses and assuming unity quantum efficiency, we estimate the upper limit of the injected carrier density to range from $\approx 3.9 \times 10^{20}$ cm^{-3} for a fluence of 1910 μJ cm^{-2} to 2.0×10^{20} cm^{-3} for a fluence of 950 μJ cm^{-2}, nearly two orders of magnitude higher than those experimentally observed at the peak of photoconductivity ($2.2–4 \times 10^{18}$ cm^{-3}, figure 4(a)). This suggests that most optically injected carriers are trapped and/or recombine due to fast nonlinear processes dominant at high carrier densities, such as Auger recombination, at times shorter than the experimental time resolution of ~0.3ps .

4. Summary

We investigated the charge carrier transport mechanisms, as well as the electronic and optical properties of Nb_2CT_x MXene, using a combination of DFT modeling of the electronic structure as a function of different surface terminations and THz spectroscopy. Through our combined DFT calculations and ultrafast optical spectroscopy measurements, we determine that this material is metallic for all surface terminations (apart from N) while also exhibiting increased carrier mobility, and consequently enhanced conductivity, when optically excited.

DFT calculations reveal that Nb_2CT_x has a metallic band structure (i.e. no band gap at E_F) for O, F, OH, Cl, Br, I or mixed OH/F and O/OH terminations, independent of their ratios. Of the studied terminations, the only one that results in the opening of a small band gap (0.66 eV) is the pure N-terminations. Earlier reported XPS results do not show evidence of N terminations, thus predicting non-zero intrinsic free carrier density and metallic nature of Nb_2CT_x. In agreement with this prediction, THz-TDS measurements reveal an intrinsic carrier density of $(1.6 \pm 0.3) \times 10^{20}$ cm^{-3} with carriers strongly

localized due to disorder and nanoflake boundaries. Short-range, intraflake free carrier mobility is found to be 30 ± 4 cm^2 V^{-1} s^{-1}, while the flake boundaries and disorder suppress the long-range (inter-flake) mobility to 2.4 ± 0.4 cm^2 V^{-1} s^{-1}. Zero-frequency (DC) conductivity found by extrapolating the fit to the experimental THz conductivity, 62 ± 15 Ω^{-1} cm^{-1}, is in good agreement with our four-point probe measurements.

We also demonstrate that photoexcitation with 1.55 eV optical pump pulses result in a rapid enhancement in photoconductivity through a combination of inter-band injection of a new population of free charge carriers and intraband excitation of intrinsic carriers. Most of the photoinjected carriers recombine within a few ps, but ∼10%–20% of photoinjected carriers persist for hundreds of ps. Rapid, over sub-ps, initial decay of photoinduced conductivity, where photoexcited carriers transfer energy to the crystal lattice, underlies the exceptionally efficient photothermal conversion efficiency that has been reported for this MXene. It can also be leveraged in high-speed photonic and optoelectronic devices.

Data availability statement

The data cannot be made publicly available upon publication because no suitable repository exists for hosting data in this field of study. The data that support the findings of this study are available upon reasonable request from the authors.

Acknowledgments

Approved for public release by DEVCOM Soldier Center: PAO#PR2024-906. This work was supported in part by NSF DMR 2018326 and 1740795 awards and by the US Army DEVCOM Soldier Center AA1 basic research program. AMF and ES acknowledge support from the NSF under the NRT-HDR-2021871 fellowship grant.

ORCID iDs

Andrew M Fitzgerald https://orcid.org/0009-0003-3637-2682
Emily Sutherland https://orcid.org/0009-0002-5726-371X
Julia L Martin https://orcid.org/0000-0001-7609-9922
Erika Colin-Ulloa https://orcid.org/0000-0002-2697-4458
Ronald L Grimm https://orcid.org/0000-0003-0407-937X
Joshua R Uzarski https://orcid.org/0000-0002-5971-1670
Michel W Barsoum https://orcid.org/0000-0001-7800-3517
N Aaron Deskins https://orcid.org/0000-0002-0041-7960
Lyubov V Titova https://orcid.org/0000-0002-2146-9102
Kateryna Kushnir Friedman https://orcid.org/0000-0002-3700-6962

References

[1] Naguib M, Kurtoglu M, Presser V, Lu J, Niu J, Heon M, Hultman L, Gogotsi Y and Barsoum M W 2011 Two-dimensional nanocrystals produced by exfoliation of Ti_3AlC_2 *Adv. Mater.* **23** 4248–53
[2] Shahzad F, Alhabeb M, Hatter C B, Anasori B, Man Hong S, Koo C M and Gogotsi Y 2016 Electromagnetic interference shielding with 2D transition metal carbides (MXenes) *Science* **353** 1137–40
[3] Rajavel K, Yu X, Zhu P, Hu Y, Sun R and Wong C 2021 Investigation on the structural quality dependent electromagnetic interference shielding performance of few-layer and lamellar Nb_2CT_x MXene nanostructures *J. Alloys Compd.* **877** 160235
[4] Hantanasirisakul K and Gogotsi Y 2018 Electronic and optical properties of 2D transition metal carbides and nitrides (MXenes) *Adv. Mater.* **30** 1804779
[5] Ghidiu M, Lukatskaya M R, Zhao M-Q, Gogotsi Y and Barsoum M W 2014 Conductive two-dimensional Titanium Carbide 'clay' with high volumetric capacitance *Nature* **516** 78–81
[6] Mashtalir O, Naguib M, Mochalin V N, Dall'Agnese Y, Heon M, Barsoum M W and Gogotsi Y 2013 Intercalation and delamination of layered carbides and carbonitrides *Nat. Commun.* **4** 1716
[7] Dillon A D, Ghidiu M J, Krick A L, Griggs J, May S J, Gogotsi Y, Barsoum M W and Fafarman A T 2016 Highly conductive optical quality solution-processed films of 2D titanium carbide *Adv. Funct. Mater.* **26** 4162–8
[8] Naguib M, Halim J, Lu J, Cook K M, Hultman L, Gogotsi Y and Barsoum M W 2013 New two-dimensional Niobium and Vanadium Carbides as promising materials for Li-Ion batteries *J. Am. Chem. Soc.* **135** 15966–9
[9] Eames C and Islam M S 2014 Ion intercalation into two-dimensional transition-metal carbides: global screening for new high-capacity battery materials *J. Am. Chem. Soc.* **136** 16270–6
[10] Liu R, Cao W, Han D, Mo Y, Zeng H, Yang H and Li W 2019 Nitrogen-doped Nb_2CT_x MXene as anode materials for lithium ion batteries *J. Alloys Compd.* **793** 505–11
[11] Zhao J, Wen J, Xiao J, Ma X, Gao J, Bai L, Gao H, Zhang X and Zhang Z 2021 Nb_2CT_x MXene: high capacity and ultra-long cycle capability for lithium-ion battery by regulation of functional groups *J. Energy Chem.* **53** 387–95
[12] Zhang W, Jin H and Zhang J 2021 Nb_2CT_x MXene as high-performance energy storage material with Na, K, and liquid K–Na alloy anodes *Langmuir* **37** 1102–9
[13] Yuan Z, Wang L, Li D, Cao J and Han W 2021 Carbon-reinforced Nb_2CT_x MXene/MoS_2 nanosheets as a superior rate and high-capacity anode for sodium-ion batteries *ACS Nano* **15** 7439–50
[14] Sarycheva A, Makaryan T, Maleski K, Satheeshkumar E, Melikyan A, Minassian H, Yoshimura M and Gogotsi Y 2017 Two-dimensional titanium carbide (MXene) as surface-enhanced raman scattering substrate *J. Phys. Chem.* C **121** 19983–8
[15] Chaudhuri K, Alhabeb M, Wang Z, Shalaev V M, Gogotsi Y and Boltasseva A 2018 Highly broadband absorber using plasmonic titanium carbide (MXene) *ACS Photonics* **5** 1115–22
[16] Velusamy D B, El-Demellawi J K, El-Zohry A M, Giugni A, Lopatin S, Hedhili M N, Mansour A E, Fabrizio E D,

Mohammed O F and Alshareef H N 2019 MXenes for plasmonic photodetection *Adv. Mater.* **31** 1807658
[17] Montazeri K, Currie M, Verger L, Dianat P, Barsoum M W and Nabet B 2019 Beyond gold: spin-coated Ti_3C_2-based MXene photodetectors *Adv. Mater.* **31** 1903271
[18] Maleski K, Shuck C E, Fafarman A T and Gogotsi Y 2021 The broad chromatic range of two-dimensional transition metal carbides *Adv. Opt. Mater.* **9** 2001563
[19] Gao L, Ma C, Wei S, Kuklin A V, Zhang H and Ågren H 2021 Applications of few-layer Nb_2C MXene: narrow-band photodetectors and femtosecond mode-locked fiber lasers *ACS Nano* **15** 954–65
[20] Li G, Liu J, Wang F, Nie H, Wang R, Yang K, Zhang B and He J 2021 Third-order nonlinear optical response of few-layer MXene Nb_2C and applications for square-wave laser pulse generation *Adv. Mater. Interfaces* **8** 2001805
[21] Kumar A N and Pal K 2022 Amine-functionalized stable Nb_2CT_x MXene toward room temperature ultrasensitive NO_2 *Gas Sensor. Mater. Adv.* **3** 5151–62
[22] Shabana N, Ankitha M, Arjun A M and Rasheed P A 2022 In-situ decoration of platinum nanoparticles on Nb_2CT_x MXene: an electrochemical sensor for L-cysteine and an efficient catalyst for oxygen evolution reaction *ECS J. Solid State Sci. Technol.* **11** 127002
[23] Lin H, Gao S, Dai C, Chen Y and Shi J 2017 A two-dimensional biodegradable niobium carbide (MXene) for photothermal tumor eradication in NIR-I and NIR-II biowindows *J. Am. Chem. Soc.* **139** 16235–47
[24] Han X, Jing X, Yang D, Lin H, Wang Z, Ran H, Li P and Chen Y 2018 Therapeutic mesopore construction on 2D Nb_2C MXenes for targeted and enhanced chemo-photothermal cancer therapy in NIR-II biowindow *Theranostics* **8** 4491–508
[25] Xuan J, Wang Z, Chen Y, Liang D, Cheng L, Yang X, Liu Z, Ma R, Sasaki T and Geng F 2016 Organic-base-driven intercalation and delamination for the production of functionalized titanium carbide nanosheets with superior photothermal therapeutic performance *Angew. Chem., Int. Ed.* **55** 14569–74
[26] Dai C, Chen Y, Jing X, Xiang L, Yang D, Lin H, Liu Z, Han X and Wu R 2017 Two-dimensional tantalum carbide (MXenes) composite nanosheets for multiple imaging-guided photothermal tumor ablation *ACS Nano* **11** 12696–712
[27] Li R, Zhang L, Shi L and Wang P 2017 MXene Ti_3C_2: an effective 2D light-to-heat conversion material *ACS Nano* **11** 3752–9
[28] Zhao Y, Hao H, Zhong J, Jiang S, Zhang G, Bi J, Yan S and Hou H 2023 Photothermocatalytic sterilization performance and mechanism of pure Nb_2CT_x MXenes nanosheets under infrared light irradiation *Appl. Surf. Sci.* **613** 155990
[29] Chen J *et al* 2022 Tailored hydrogel delivering niobium carbide boosts ROS-scavenging and antimicrobial activities for diabetic wound healing *Small* **18** 2201300
[30] Wang Y *et al* 2023 2D Nb_2CT_x MXene/MoS_2 heterostructure construction for nonlinear optical absorption modulation *Opt.-Electron. Adv.* **6** 220162-1-220162-11
[31] Li G, Kushnir K, Dong Y, Chertopalov S, Rao A M, Mochalin V N, Podila R and Titova L V 2018 Equilibrium and non-equilibrium free carrier dynamics in 2D $Ti_3C_2T_x$ MXenes: tHz spectroscopy study *2D Mater.* **5** 035043
[32] Zheng W *et al* 2022 Band transport by large Fröhlich polarons in MXenes *Nat. Phys.* **18** 544–50
[33] Colin-Ulloa E, Fitzgerald A, Montazeri K, Mann J, Natu V, Ngo K, Uzarski J, Barsoum M W and Titova L V 2023 Ultrafast spectroscopy of plasmons and free carriers in 2D MXenes *Adv. Mater.* **35** 2208659
[34] Shao Y, Zhang F, Shi X and Pan H 2017 N-functionalized MXenes: ultrahigh carrier mobility and multifunctional properties *Phys. Chem. Chem. Phys.* **19** 28710–7
[35] Gao L *et al* 2020 Ultrafast relaxation dynamics and nonlinear response of few-layer niobium carbide MXene *Small Methods* **4** 2000250
[36] Natu V, Pai R, Wilson O, Gadasu E, Badr H, Karmakar A, Magenau A J D, Kalra V and Barsoum M W 2022 Effect of base/nucleophile treatment on interlayer ion intercalation, surface terminations, and osmotic swelling of $Ti_3C_2T_z$ MXene multilayers *Chem. Mater.* **34** 678–93
[37] Natu V and Barsoum M W 2023 MXene surface terminations: a perspective *J. Phys. Chem.* C **127** 20197–206
[38] Li Y *et al* 2020 A general Lewis acidic etching route for preparing MXenes with enhanced electrochemical performance in non-aqueous electrolyte *Nat. Mater.* **19** 894–9
[39] Arole K, Blivin J W, Bruce A M, Athavale S, Echols I J, Cao H, Tan Z, Radovic M, Lutkenhaus J L and Green M J 2022 Exfoliation, delamination, and oxidation stability of molten salt etched Nb_2CT_z MXene nanosheets *Chem. Commun.* **58** 10202–5
[40] Liu L, Orbay M, Luo S, Duluard S, Shao H, Harmel J, Rozier P, Taberna P-L and Simon P 2022 Exfoliation and delamination of $Ti_3C_2T_x$ MXene prepared via molten salt etching route *ACS Nano* **16** 111–8
[41] Kamysbayev V, Filatov A S, Hu H, Rui X, Lagunas F, Wang D, Klie R F and Talapin D V 2020 Covalent surface modifications and superconductivity of two-dimensional metal carbide MXenes *Science* **369** 979–83
[42] Bai Y, Liu C, Chen T, Li W, Zheng S, Pi Y, Luo Y and Pang H 2021 MXene-copper/cobalt hybrids via Lewis acidic molten salts etching for high performance symmetric supercapacitors *Angew. Chem., Int. Ed.* **60** 25318–22
[43] Li G, Amer N, Hafez H A, Huang S, Turchinovich D, Mochalin V N, Hegmann F A and Titova L V 2020 Dynamical control over terahertz electromagnetic interference shielding with 2D $Ti_3C_2T_y$ MXene by ultrafast optical pulses *Nano Lett.* **20** 636–43
[44] Li G, Natu V, Shi T, Barsoum M W and Titova L V 2020 Two-dimensional MXenes $Mo_2Ti_2C_3T_z$ and $Mo_2TiC_2T_z$: microscopic conductivity and dynamics of photoexcited carriers *ACS Appl. Energy Mater.* **3** 1530–9
[45] Li E *et al* 2024 Charge carriers localization effect revealed through terahertz spectroscopy of MXene: $Ti_3C_2T_x$ *Small* **20** 2306200
[46] Kresse G and Hafner J 1994 Ab initio molecular-dynamics simulation of the liquid-metal–amorphous-semiconductor transition in germanium *Phys. Rev.* B **49** 14251–69
[47] Kresse G and Hafner J 1993 Ab initio molecular dynamics for liquid metals *Phys. Rev.* B **47** 558–61
[48] Kresse G and Furthmüller J 1996 Efficient iterative schemes for ab initio total-energy calculations using a plane-wave basis set *Phys. Rev.* B **54** 11169–86
[49] Kresse G and Furthmüller J 1996 Efficiency of ab-initio total energy calculations for metals and semiconductors using a plane-wave basis set *Comput. Mater. Sci.* **6** 15–50
[50] Perdew J P, Burke K and Ernzerhof M 1996 Generalized gradient approximation made simple *Phys. Rev. Lett.* **77** 3865–8
[51] Blöchl P E 1994 Projector augmented-wave method *Phys. Rev.* B **50** 17953–79
[52] Kresse G and Joubert D 1999 From ultrasoft pseudopotentials to the projector augmented-wave method *Phys. Rev.* B **59** 1758–75
[53] Heyd J, Scuseria G E and Ernzerhof M 2003 Hybrid functionals based on a screened Coulomb potential *J. Chem. Phys.* **118** 8207–15
[54] Wang V, Xu N, Liu J-C, Tang G and Geng W-T 2021 VASPKIT: a user-friendly interface facilitating high-throughput computing and analysis using VASP code *Comput. Phys. Commun.* **267** 108033
[55] VahidMohammadi A, Rosen J and Gogotsi Y 2021 The world of two-dimensional carbides and nitrides (MXenes) *Science* **372** eabf1581
[56] Caffrey N M 2018 Effect of mixed surface terminations on the structural and electrochemical properties of two-dimensional $Ti_3C_2T_x$ and V_2CT_x MXenes multilayers *Nanoscale* **10** 13520–30

[57] Wang X, Shen X, Gao Y, Wang Z, Yu R and Chen L 2015 Atomic-scale recognition of surface structure and intercalation mechanism of $Ti_3C_2T_x$ *J. Am. Chem. Soc.* **137** 2715–21
[58] Zha X-H, Luo K, Li Q, Huang Q, He J, Wen X and Du S 2015 Role of the surface effect on the structural, electronic and mechanical properties of the carbide MXenes *Europhys. Lett.* **111** 26007
[59] Hu J, Xu B, Ouyang C, Zhang Y and Yang S A 2016 Investigations on Nb_2C monolayer as promising anode material for Li or non-Li ion batteries from first-principles calculations *RSC Adv.* **6** 27467–74
[60] Jepsen P U, Cooke D G and Koch M 2011 Terahertz spectroscopy and imaging—modern techniques and applications *Laser Photonics. Rev.* **5** 124–66
[61] Cocker T L *et al* 2010 Terahertz conductivity of the metal-insulator transition in a nanogranular VO_2 film *Appl. Phys. Lett.* **97** 221905
[62] Baxter J B and Schmuttenmaer C A 2009 Carrier dynamics in bulk ZnO. I. Intrinsic conductivity measured by terahertz time-domain spectroscopy *Phys. Rev.* B **80** 235205
[63] Cooke D G 2022 Terahertz photoconductivity *Photoconductivity and Photoconductive Materials* (Wiley) pp 369–98
[64] Neu J and Schmuttenmaer C A 2018 Tutorial: an introduction to terahertz time domain spectroscopy (THz-TDS) *J. Appl. Phys.* **124** 231101
[65] Ulbricht R, Hendry E, Shan J, Heinz T F and Bonn M 2011 Carrier dynamics in semiconductors studied with time-resolved terahertz spectroscopy *Rev. Mod. Phys.* **83** 543–86
[66] Butler K T, Dringoli B J, Zhou L, Rao P M, Walsh A and Titova L V 2016 Ultrafast carrier dynamics in $BiVO_4$ thin film photoanode material: interplay between free carriers, trapped carriers and low-frequency lattice vibrations *J. Mater. Chem.* A **4** 18516–23
[67] Titova L V, Cocker T L, Xu S, Baribeau J-M, Wu X, Lockwood D J and Hegmann F A 2016 Ultrafast carrier dynamics and the role of grain boundaries in polycrystalline silicon thin films grown by molecular beam epitaxy *Semicond. Sci. Technol.* **31** 105017
[68] Lloyd-Hughes J and Jeon T-I 2012 A review of the terahertz conductivity of bulk and nano-materials *J. Infrared Millim. Terahertz Waves* **33** 871–925
[69] Yang Y and Ting C S 2020 Electronic structures and electron–phonon superconductivity of Nb_2C-based MXenes *J. Phys. D: Appl. Phys.* **53** 485301
[70] Khazaei M, Arai M, Sasaki T, Chung C-Y, Venkataramanan N S, Estili M, Sakka Y and Kawazoe Y 2013 Novel electronic and magnetic properties of two-dimensional transition metal carbides and nitrides *Adv. Funct. Mater.* **23** 2185–92
[71] Yusupov K, Björk J and Rosen J 2023 A systematic study of work function and electronic properties of MXenes from first principles *Nanoscale Adv.* **5** 3976–84
[72] Shao Y 2020 *MXene-Based Materials for Energy Conversion/Storage and Device Applications: A First-Principles Study* (University of Macau) pp 164
[73] Grischkowsky D, Keiding S, van Exter M and Fattinger C 1990 Far-infrared time-domain spectroscopy with terahertz beams of dielectrics and semiconductors *J. Opt. Soc. Am.* B **7** 2006–15
[74] Naftaly M and Miles R E 2007 Terahertz time-domain spectroscopy for material characterization *Proc. IEEE* **95** 1658–65
[75] Richter C and Schmuttenmaer C A 2010 Exciton-like trap states limit electron mobility in TiO_2 nanotubes *Nat. Nanotechnol.* **5** 769–72
[76] Alberding B G, DeSario P A, So C R, Dunkelberger A D, Rolison D R, Owrutsky J C and Heilweil E J 2017 Static and time-resolved terahertz measurements of photoconductivity in solution-deposited ruthenium dioxide nanofilms *J. Phys. Chem.* C **121** 4037–44
[77] Walther M, Cooke D G, Sherstan C, Hajar M, Freeman M R and Hegmann F A 2007 Terahertz conductivity of thin gold films at the metal-insulator percolation transition *Phys. Rev.* B **76** 125408
[78] Smith N V 2001 Classical generalization of the Drude formula for the optical conductivity *Phys. Rev.* B **64** 155106
[79] Valdes L B 1954 Resistivity measurements on germanium for transistors *Proc. IRE* **42** 420–7
[80] Smits F M 1958 Measurement of sheet resistivities with the four-point probe *Bell Syst. Tech. J.* **37** 711–8